NJC

PAPER

Check for updates

Functionalized graphene nanoplatelets: a promising adsorbent for solid-phase uranium extraction†

Aline Dressler, Antoine Leydier ✪ * and Agnès Grandjean ✪

Graphene nanoplatelets (GNPs) were functionalized with an organic ligand to prepare materials for selective extraction of uranium from acidic solution. The effects of di-2-ethylhexylcarbamoylethylbutyl phosphonate (DEHCEBP) ligand concentration on the structure of the final solids and the effect on its extraction capacity were investigated in materials with 0.3, 0.5, 0.8, 1.0 and 1.2 mmol of organic ligand per gram of solid. Raman spectroscopy and X-ray diffraction analysis confirm that impregnation does not modify the carbon network and interlayer distance of the GNPs. As shown with nitrogen adsorption–desorption experiments, the amidophosphonate ligand first fills the micropores then the mesopores of the support while the ligand concentration increases. Acidic uranium solutions with high sulfate content were used to simulate the composition of ore treatment leaching solutions. Increasing the ligand concentration inside the graphene leads to an increase of the equilibration time in batch extraction experiments. This suggests that the DEHCEBP molecules form multiple layers in the materials containing the highest ligand contents. The results also suggest that the ligands located inside the micropores remain inaccessible for extraction. Maximum extraction capacities of the material with 1.2 mmol g^{-1} to 0.3 mmol g^{-1} DEHCEBP ranged respectively from 108 mg to 18 mg of uranium per gram of solid. This indicates the high potential of these functionalized graphene nanoplatelets for solid phase uranium extraction.

Introduction

High performance adsorbents are required for various applications, such as water or wastewater treatment[1,2] and metal extraction.[3] Specific properties are required for each application but a high capacity, high uptake rate, prolonged retention and reusability are sought after in all adsorbents.

We have previously shown that impregnation to functionalize silica is an efficient and easy way to obtain a selective sorbent.[4–8] Silica was impregnated by bifunctional amidophosphonate ligands developed for the solvent extraction of uranium from acidic solutions (both phosphate[9,10] and sulfate[11]). These studies show a complexation of uranium by phosphonate groups with various complexes depending on the ligand, on the process and on the acidic solution (sulfuric or phosphoric).[12] These studies and other results for strontium[13] and CO_2 adsorption[14,15] show that impregnated materials generally have higher adsorption capacities than grafted ones, presumably

because of the absence of conformational constraints. More recently,[16] we observed in a series of silica-based uranium extractants impregnated with 10–20 wt% amidophosphonate ligand that a higher ligand concentration had a negative impact on the extraction kinetics.

The maximum extraction capacity is closely linked to the surface area of the support. To increase this extraction capacity, without decreasing the efficiency of the process, we need to use a support with a high specific surface allowing high amidophosphonate impregnation rates. Graphene-based materials have gained a lot of attention in this context because they can easily be modified with specific functional groups.[17] Along with their chemical stability[18] and high specific surface areas (up to 2630 m^2 g^{-1} in theory),[19] these characteristics allow the development of hybrid materials with high extraction capacities. However, robust procedures for the large-scale synthesis of single- or few-layer pure graphene are lacking, and the outstanding performances measured in research laboratories have so far not been achieved using mass-produced materials.[20,21]

Graphene nanoplatelets are a mixture of single-layer, few-layer, and nanostructured graphite[22] and are also known as graphite nanoplatelets. Their specific structure and their low costs when produced in large quantities make them an

CEA, DES, ISEC, DMRC, Univ. Montpellier, Marcoule, France.
E-mail: antoine.leydier@cea.fr

† Electronic supplementary information (ESI) available. See DOI: https://doi.org/10.1039/d3nj04415g

attractive alternative for adsorption applications.[23–25] As such, GNPs have found applications in the absorption of organic pollutants,[26–29] solar cells,[30] and in various polymer nano-composites with flame retardant,[31] shape memory[32] and gas barrier[33] properties.

The lateral size and thickness of the flakes, and the density of defects and impurities in GNPs depend on the manufacturing technique,[34,35] and their selectivity and extraction capacity can be improved by the nature of the functionalization. Surface functionalization by covalent attachment involves rehybridization of one or more of the sp² carbons in the network into the sp³ configuration, with a simultaneous loss of electronic conjugation.[36] Non-covalent functionalization involves three main interactions including hydrophobic interactions, and van der Waals and electrostatic forces.[36–38] For post-synthesis functionalization with organic molecules, GNPs do in general have residual oxygen-containing groups but these are not reactive enough for the grafting of organic groups.[37] On the other hand, while non-covalent functionalization can be achieved without functional groups, the molecule must be sufficiently attracted to the graphene surface to remain attached.[38]

Here, graphene-based adsorbents were developed for uranium extraction during the uranium recovery stage from mines. These operations typically involve first ore leaching and then selective extraction of uranium from the leaching solution followed by a concentration step.[39–41] Solid-phase extraction (SPE) is an alternative to solvent extraction processes for the selective recovery of low-concentration uranium (up to 1 g L⁻¹) because of the absence of solvent, lower processing times and lower costs.[42,43] Solid-phase extraction is also a more compact process, allowing extraction and back-extraction to be performed in separate locations. The uranium industry already uses solid-phase extractants, as for example the resin-in-pulp process, or using organic resin based on ion exchange. However, in the case of high sulfate concentrations and/or in the presence of a high concentration of competing cations in the leaching solution, solid-phase extraction is less efficient and solvent extraction is preferred. The use of a selective ligand linked to a support is the first way to improve the SPE process. In the literature, numerous materials, based on metal oxide particles,[44,45] mesoporous silica,[46,47] carbon supports,[48–51] MOFs,[52–54] fibers[55,56] or resins[41,57–59] were suggested and evaluated for the removal of uranium ions from aqueous effluents by a SPE process.

In the present study, amidophosphonate ligands were impregnated in commercial GNPs. The non-polar sp² carbon surface of GNPs allows these ligands to be impregnated without prefunctionalization and their high pore volume translates into a high loading capacity. In SPE, however, the accessibility of the ligand molecules is strongly dependent on their arrangement inside the pores of the materials and the mesostructure of the mineral solid support.[60] We therefore studied the effects of the ligand concentration on the structure of the functionalized materials and then we assessed the effect of the support on the material extraction properties.

Materials and methods

Chemicals

All organic reagents were used as received from Aldrich, Acros and Fluka. Solvents were purchased from Acros, Pro-Labo, Fluka, and Aldrich. Anhydrous solvents were obtained from Acros.

Materials synthesis

The organic ligand (see Fig. S1, ESI†) di-2-ethylhexylcarbamoyl-ethylbutyl phosphonate (DEHCEBP) was synthesized as described by Turgis et al.[61] Commercial graphene nanoplatelets (grade C, purchased from Aldrich) were then functionalized by wet impregnation. About 2 g of GNPs were mixed with 20 mL of dichloromethane containing the desired amount of DEHCEBP in a 50 mL round bottom flask for 24 h. After evaporation of the solvents and 12 h of vacuum drying, the final materials were obtained. The materials were named as follows: Imp-X/@GNPs, where X = 0.3, 0.5, 0.8, 1.0 or 1.2 represents the concentration of DEHCEBP in mmol per gram of the total functionalized solid.

Uranium-containing solution

The simulated ore leaching solutions were obtained using a solution with high sulfate concentration (146 g L⁻¹; $[SO_4^{2-}]/[U]$ = 900 mol mol⁻¹) and 400 mg L⁻¹ uranium. Adding sulfuric acid allows the pH to be adjusted to 1. The desired $[SO_4^{2-}]/[U]$ ratio was obtained by adding sodium sulfate.

Characterization of the organic ligand

Solution ¹H, ³¹P and ¹³C NMR spectra were recorded on a Bruker 400 ultrashield VS spectrometer (Larmor frequencies, 400.13 MHz for ¹H, 161.976 MHz for ³¹P, 100.613 MHz for ¹³C) using deuterated chloroform as the solvent and internal standard. Mass spectrometry analyses were performed on a Bruker Micro Q tof Mass spectrometer.

The characteristics of the ligand are presented in Fig. S2 and S3 (mass spectra) and S4–S6 (NMR spectra) (ESI†).

Characterization of the materials

Ligand concentrations per unit mass of solid (τ_L, mmol g⁻¹) were calculated assuming that the total organic content added at the impregnation step was incorporated into the solid support. This assumption was validated by gravimetric analysis, using dichloromethane to dissolve the organic ligand, and by thermogravimetric analysis (TGA, TGA/DSC 1, Mettler Toledo).

For the TGA experiments, about 20 mg of the functionalized material was placed in a 70 µL alumina pan and heated from 30 to 1000 °C at 5 °C min⁻¹ under a 30 mL min⁻¹ air flow. The ligand concentrations were calculated using eqn (1):

$$\tau_L = \frac{m_i - m_f}{M_L} \times cf \qquad (1)$$

where m_i and m_f are respectively the mass (mg) of the functionalized support at 150 and 300 °C, M_L is the molar mass (mol g⁻¹) of the organic ligand and cf is the correction factor. With the initial temperature of this range fixed at 150 °C,
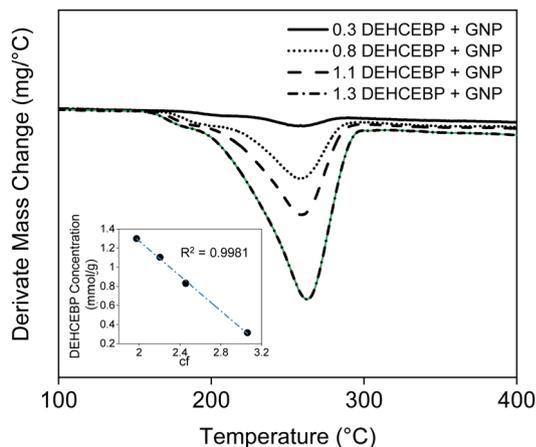
Fig. 1 Differential thermogravimetric curves of the GNPs and DEHCEBP mixtures, with 0.3, 0.8, 1.1 and 1.3 mmol g^{-1} DEHCEBP. The inset shows the linear relationship between the correction factor and the DEHCEBP concentration. Note that the analyzed samples are not the impregnated materials, but simple mixtures of the components used to calculate the correction factor.

the loss of mass is only due the decomposition of the ligand. Indeed, below 150 °C, the ligand is thermally stable and the loss of mass comes from the evaporation of physisorbed water (Fig. S5, ESI†). Although the ligand is not completely calcined under these conditions, the temperature of 300 °C is within a mass loss plateau (Fig. 1). The correction factor was therefore determined as follows, to avoid underestimating the ligand content. TGA experiments were repeated with different masses of GNPs and amidophosphonate ligand in the alumina pan and the weight loss of the system was measured as described above. The correction factor was then calculated by comparing the values obtained by TGA with the real amounts of amidophosphonate ligand present in the mixture (eqn (2)),

$$ cf = \frac{m_L/(m_G + m_L)}{(m_{tga,i} - m_{tga,f})/m_i} \tag{2} $$

where m_{tgaL} and m_{tgaG} are respectively the masses (mg) of the DEHCEBP ligand and GNPs in the pan and $m_{tga,i}$ and $m_{tga,f}$ are the masses (mg) measured by TGA at 150 and 300 °C. This method using TGA and the correction factor is an easy way to determine the ligand concentration inside a solid material with limited stability at high temperature.

The ligand concentrations obtained from the TGA analysis, using eqn (1), were equal to the amounts of DEHCEBP added during the synthesis of the respective materials.

Organic contents inside the materials calculated from the amount of DEHCEBP added in the impregnation process are in agreement with the results of the gravimetric and thermogravimetric analysis. The fact that all the ligand added in the preparation of the adsorbents is incorporated into the support confirms that the synthesis route is robust.

Attenuated total reflection Fourier transform infrared spectroscopy (ATR-FTIR) data were acquired using a PerkinElmer Spectrum 100 spectrometer from 615 to 4000 cm^{-1}. The scans

were quadrupled with a nominal resolution of 4 cm^{-1} and background correction (atmospheric bands) for each substrate.

Raman spectra were recorded using a Horiba Jobin Yvon device. The data were collected using a 532 nm laser (Olympus MPlan N 100×/0.90) and a 100× objective lens from 500 to 3000 cm^{-1} with an integration time of 30 s and averaged over 10 scans.

The median particle size by volume, $d(50)_v$, was determined using a laser diffraction particle size analyzer (Mastersizer 3000, Malvern Panalytical) with the refractive index and absorption set to 2.42 and 1, respectively, using water as the dispersant.[62] The experiments were carried out without ultrasonication to avoid altering the size of the GNP particles.

The unmodified GNPs and functionalized materials were observed by field emission scanning electron microscopy (FE-SEM, Quanta 200 ESEM FEG, FEI Company) under high vacuum, with a 1.8 kV accelerating voltage. Samples were dispersed in high purity water by shaking without sonication and drop cast on carbon tape without additional preparation.

The carbon interlayer spacing in the materials was determined by powder X-ray diffraction (XRD) with the Bragg Brentano geometry (PANalytical X'Pert PRO MPD; copper anode $\lambda_{K\alpha1}$ = 1.54056 Å generated at 45 mA and 40 kV, X'celerator detector). The XRD patterns were collected over the 2θ range of 10–70° with 0.017° steps and a measurement time of 0.625 s per step.

Nitrogen adsorption–desorption isotherms were measured at −196 °C using a Micromeritics ASAP 2020 surface area and pore size analyzer. The samples were degassed at 90 °C for 24 h before analysis. The Brunauer–Emmett–Teller (BET) method was used to calculate the specific surface areas. Total pore volumes were determined using the volume of adsorbed gas at $P/P_0 \approx 1$. Micropore volumes were taken at $P/P_0 = 0.05$ and mesopore volumes were then deduced by subtracting the micropore volume from the total pore volume. This procedure allows the evaluation of the percentage of the volume of each pore type (micro and meso) occupied by the ligand.

The surface density ($d_{sLigand}$) of the ligand (DEHCEBP nm^{-2}) was calculated from the BET-specific surface area S_{BET} (m^2 g^{-1}) of the pristine support and the organic content (τ_L, mmol g^{-1}, from eqn (1)) of the final materials using eqn (3):

$$ d_{sLigand} = \frac{\tau_L \times N_A}{S_{BET} \times 10^{18}} \tag{3} $$

The area occupied by a single DEHCEBP molecule was estimated using the empirical Tanford formula for the length (r, in nm) of a simple hydrocarbon chain of n atoms:

$$ r = 0.154 + 0.1265n \tag{4} $$

Uranium extraction experiments. The kinetics of U(VI) removal using the synthesized adsorbents was studied in batch experiments at 25 °C with shaking. The same solid/liquid ratio ($\Psi_{S/L}$) of about 2.5 mg mL^{-1} was used for all experiments. Each point in the kinetics curves corresponds to a single experiment.

After the chosen contact times, and filtration through a 0.22 μm cellulose acetate membrane, the uranium concentration in the liquid phase was measured by inductively coupled plasma atomic emission spectroscopy (ICP-AES; 2% nitric acid; Analytik Jena PlasmaQuant PQ 9000). The mass or amount of uranium extracted per unit mass of solid, that is the extraction capacity at the chosen duration time ($Q_U(t)$,) was calculated using eqn (5):

$$Q_U(t) = [U_i - U_t] \times \frac{V}{m} \qquad (5)$$

where U_i and U_t (mg L^{-1} or mmol L^{-1}) are respectively the uranium concentrations in the solution before contact and after contact during the duration time t between the solid and the solution, V is the volume of the solution (L) and m is the mass of the solid sample (g).

The ligand to uranium molar ratio (L/U) in each material under these experimental conditions was determined using the measured ligand concentrations (τ_L, mmol g^{-1}) inside each solid support, L/U = $\tau_L/Q_U(t)$.

If all ligand molecules are accessible for extraction, L/U corresponds to the stoichiometric coefficient of the complexes between the ligand and uranium formed inside the pores of the material during extraction.

The phosphorous concentration in the liquid phase after contact with the synthesized materials was also measured by ICP-AES (2% nitric acid; Analytik Jena PlasmaQuant PQ 9000) to determine the amount of ligand leached during the extraction process at different contact times.

Results and discussion

Chemical characterization

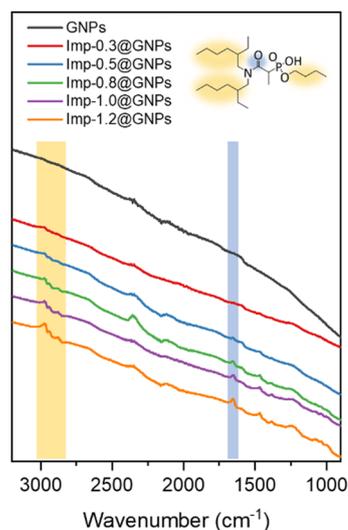The FTIR spectra of the impregnated materials (Fig. 2) show peaks corresponding to the organic ligand at 1655 cm^{-1} (C=O stretching, amide) and between 2980 and 2850 cm^{-1} (C–H stretching, alkane), confirming that carbamoylphosphonate molecules are present on the pore surface of the graphene nanoplatelets.

The Raman spectra of the unmodified GNPs and impregnated materials show the three characteristic peaks of graphene (Fig. 3), which provide information on defects (the D band at ~1340 cm^{-1}), in-plane vibrations of sp^2 carbon atoms (the G band at ~1570 cm^{-1}) and the stacking order (the 2D band at ~2700 cm^{-1}).[63] The position and shape of the three peaks are sensitive to the arrangement of the graphene layers and the level of charge-doping.[64,65] In contrast with the results obtained for the GNP-based materials, monolayer graphene has a sharp 2D peak.[66] The intensity ratio of the D and G bands (I_D/I_G) is often used to estimate the defect concentration in carbon materials.[63] The fact that the I_D/I_G ratio does not change significantly after impregnation is a sign of a very poor interaction between ligand and GNP. Indeed, the synthesis route uses direct impregnation, without chemical reaction between the ligand and the GPN surface. Another sign of weak or non-covalent bonding between the ligand and the GPN surface comes from the fact that contacting the functionalized material in an organic solvent enables the recovery of the entire ligand.

This functionalization does not significantly alter the structural order of the GNPs,[67] unlike what has previously been observed for covalent functionalization.[68]

Morphological characterization

The median particle size ($d(50)_v$) in the materials increases with the DEHCEBP concentration (Table 1), suggesting that impregnation leads to the formation of larger agglomerates.

Particle sizes were measured by laser diffraction, a technique usually used to determine the mean lateral size of graphene oxide platelets[69] and commercial graphene materials[62] with

Fig. 2 Fourier-transform infrared spectra of the unmodified GNPs and the impregnated materials with DEHCEBP concentrations of 0.3–1.2 mmol g^{-1}.
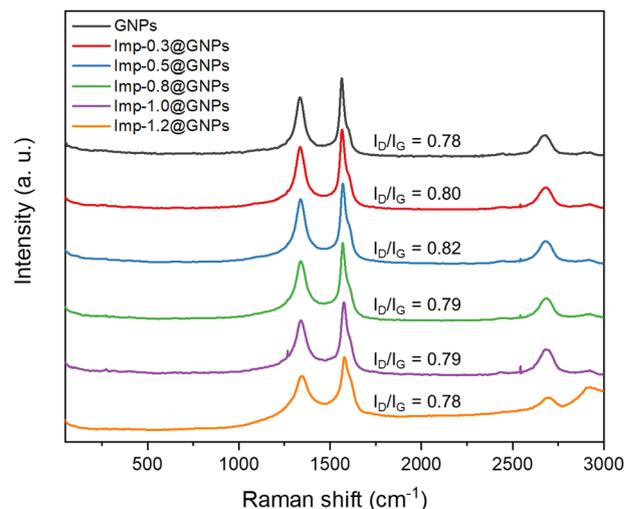

Fig. 3 Raman spectra normalized to the G peak of unmodified GNPs and the impregnated materials with DEHCEBP concentrations of 0.3–1.2 mmol g^{-1}.

Table 1 Properties of unmodified GNPs and of the different impregnated materials synthesized in this study

Material	$\tau_L{}^a$	$\%_L{}^b$	$d(50)_v{}^c$	$S_{BET}{}^d$	$V_{pores}{}^e$	$V_{micropores}{}^f$	$d_{sLigand}{}^g$
GNP			42 ($\pm$1)	675 ($\pm$34)	1.31 ($\pm$0.07)	0.25	
Imp-0.3@GNP	0.32 ($\pm$0.02)	13.9 ($\pm$0.7)	43 ($\pm$3)	302 ($\pm$15)	0.75 ($\pm$0.04)	0.09	0.29
Imp-0.5@GNP	0.52 ($\pm$0.03)	22.5 ($\pm$1.1)	72 ($\pm$3)	153 ($\pm$8)	0.63 ($\pm$0.03)	0.04	0.46
Imp-0.8@GNP	0.80 ($\pm$0.04)	34.7 ($\pm$1.7)	99 ($\pm$5)	60 ($\pm$3)	0.35 ($\pm$0.02)	0.01	0.71
Imp-1.0@GNP	1.02 ($\pm$0.05)	44.2 ($\pm$2.2)	127 ($\pm$3)	23 ($\pm$1)	0.17 ($\pm$0.01)	0.01	0.91
Imp-1.2@GNP	1.15 ($\pm$0.05)	49.8 ($\pm$2.5)	140 ($\pm$9)	6 ($\pm$1)	0.08 ($\pm$0.01)	0	1.03

^{a} Concentration (mmol g^{-1}) of DEHCEBP. ^{b} Mass percentage of DEHCEBP. ^{c} Median particle size by volume (μm). ^{d} Specific surface area (m^2 g^{-1}). ^{e} Total pore volume, measured at $P/P_0 \approx 1$ (cm^3 g^{-1}). ^{f} Micropore volume. Measured at $P/P_0 \approx 0.05$ (cm^3 g^{-1}). ^{g} Surface density of the ligand (DEHCEBP nm^{-2}) using eqn (3).

high accuracy, but that is known to underestimate the presence of smaller particles.[69]

Fig. 4 shows SEM images of pristine GNPs and the impregnated materials. Pristine GNPs form agglomerates, as reported previously.[70] Increasing the concentration of the organic ligand leads to the formation of a coating layer around the GNPs, which becomes visible on the micrographs at DEHCEBP concentrations above 0.8 mmol g^{-1} (Fig. 4d–f). The presence of organic molecules on the outer surface of the GNPs suggests that the ligand may act as a bonding agent between initially separated nanoplatelets.

This would explain the increase in the mean particle diameter with the DEHCEBP concentration measured by laser diffraction.
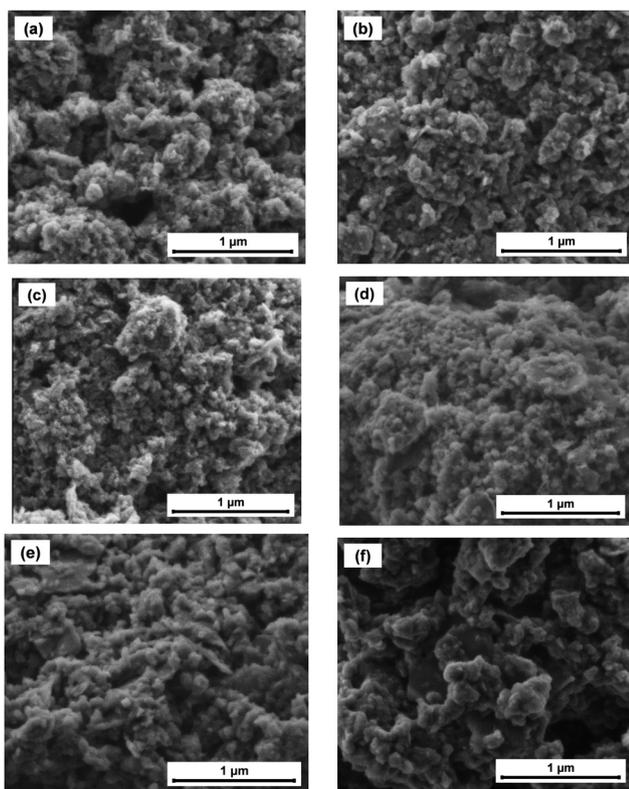
Fig. 5 compares the XRD patterns of the materials. The sharp peak at $2\theta = 26.36°$ in the data from the pristine GNPs corresponds to an interlayer distance (d_{002}) of 0.35 nm, close to that of high purity graphene ($\sim$0.34 nm).[71] This peak is also present in the data from the pristine samples but decreases in intensity with the organic content from 0.87 to 0.36 of the intensity observed for pristine GNPs between Imp-0.3 and Imp-1.2@GNPs, respectively (Fig. 5). These data show that impregnation of molecule does not affect the interlayer structure of the graphene nanoplatelets. The XRD patterns of the impregnated samples also show a broad peak at $2\theta = 20°$, indicating the presence of an amorphous phase.

Fig. 6 shows the nitrogen adsorption–desorption isotherms of the GNP support before and after impregnation with different ligand concentrations. The unmodified GNPs and the Imp-0.3, Imp-0.5 and Imp-0.8@GNPs materials have type II isotherms, with an H3 hysteresis loop, typical of particles with a porous network consisting of macropores and non-rigid aggregates of plate-like particles.[72] For Imp-1.0 and Imp-1.2@GNPs, the hysteresis loops are closer to type H4, with type I adsorption branches, typical of solids with relatively small external surface areas.[72] This can be explained by pore filling due to the high ligand concentration, and also by aggregation of the nanoplatelets as observed previously.
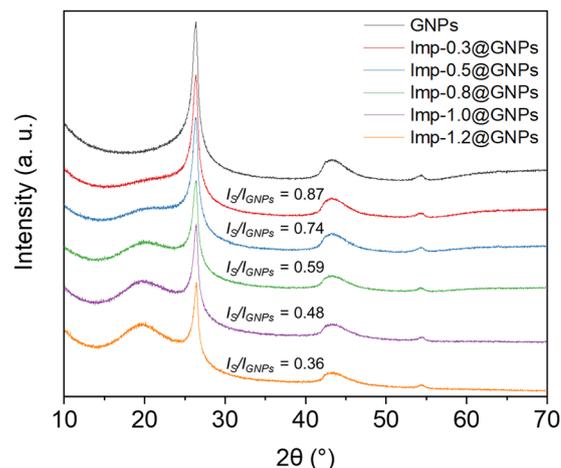

Fig. 4 Scanning electron micrographs of (a) unmodified GNPs and (b–f) impregnated GNPs with DEHCEBP concentrations of (b) 0.3, (c) 0.5, (d) 0.8, (e) 1.0 and (f) 1.2 mmol g^{-1}.

Fig. 5 X-Ray diffractograms of pristine GNPs and the DEHCEBP-impregnated materials. The Is/IGNPs ratios for the impregnated materials correspond to the relative intensity of the peak at $2\theta = 26.36°$ compared with the data from unmodified GNPs.
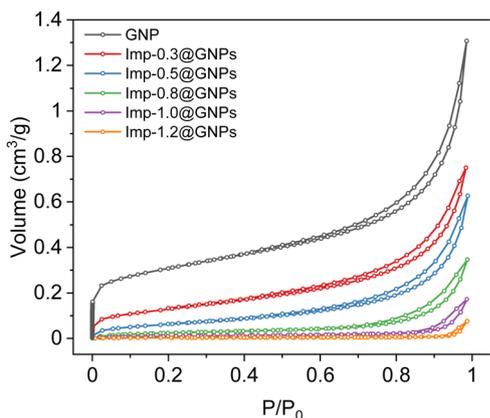
Fig. 6 Nitrogen adsorption–desorption isotherms of unmodified GNPs and of the impregnated materials with DEHCEBP concentrations of 0.3–1.2 mmol g^{-1}.

Fig. 8 Residual pore volume of the impregnated materials as a function of the concentration of organic ligand (DEHCEBP), R_2 = 0.9943.

Since unmodified GNPs have a total pore volume of 1.31 cm^3 g^{-1} and the density of DEHCEBP is about 1.0 g cm^{-3}, the maximum ligand concentration in the pore volume of this support is about 57 wt%. However, samples prepared with more than 50 wt% DEHCEBP exhibited a sticky appearance, indicating that a considerable portion of the ligands is probably localized outside the pores and that the maximum reachable loading using this procedure is about 1.2 mmol g^{-1} or 50 wt%. Some of the pores in the material, presumably the smaller ones, must therefore be inaccessible to the ligand.

The ligand concentrations, pore volumes and specific surface areas of the studied materials are listed in Table 1. The total pore volume and BET specific surface area decrease after functionalization and follow an opposite trend to the ligand concentration. This suggests that at least some of the ligand molecules are located within the pores.

Fig. 7 shows the percentage of filled micropores and mesopores with respect to the unmodified support for all the synthesized materials. The proportion of filled volume is always higher in the micropore volume than in the mesopore volume.

This suggests that the organic ligand tends to fill the micropores before the mesopores in the support, as previously observed for silica-based impregnated materials.[16] Furthermore, the fact that the pores in samples Imp-1.0 and Imp-1.2@GNPs are almost completely filled by the ligand (Fig. 7) explains why they have a very low specific surface area (Table 1).

The total (residual) pore volume of the impregnated materials decreases linearly with the DEHCEBP concentration, indicating that each ligand molecule occupies a similar volume within the pores of the support, regardless of its concentration (Fig. 8).

Following the same reasoning based on the Tanford formula (eqn (4)) as previously,[16] assuming that the movement of the impregnated ligands is not restricted and that a DEHCEBP molecule is about 2 nm long, each molecule occupies a circular area of about 3.3 nm^2. The full saturation of the surface of the solid support with one layer of ligand molecules requires theoretically about 0.3 DEHCEBP nm^{-2}. This means that the ligand molecules are disposed in a single layer on the support surface only for DEHCEBP concentrations up to 0.3 mmol g^{-1} and form multiple layers at higher concentrations.

In summary, these results suggest that during the impregnation process, at low concentrations, the ligand first partially fills the micropores and forms a monolayer in the mesopores. As the ligand concentration is increased, the remaining accessible micropores are filled and the DEHCEBP molecules tend to form multiple layers in the mesopores, the number of layers increasing with the ligand concentration (Fig. 9).

Extraction of uranium from sulfuric acid solutions

The uranium extraction capacity (Q_U, mg g^{-1}) of the five synthetized materials was measured for contact times of 5 min to 9 days in a high sulfate solution ([SO$_4^{2-}$]/[U] = 900 mol mol^{-1}). Experiments performed under the same conditions with unmodified GNPs showed that the support is not involved in uranium extraction. That means that the extraction capacity of the impregnated materials comes entirely from the amidophosphonate ligands inside the support. The selectivity of the DEHCEBP ligand impregnated on a solid support in high sulfate solutions has been demonstrated previously.[16]
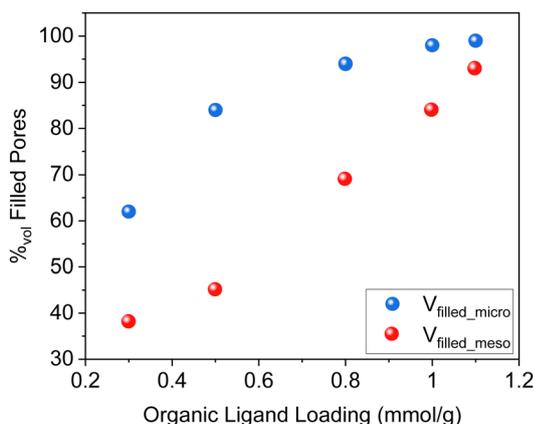

Fig. 7 Percentage of filled micropore and mesopore volume in impregnated graphene nanoplatelets as a function of the concentration of organic ligand (DEHCEBP) in the final materials.
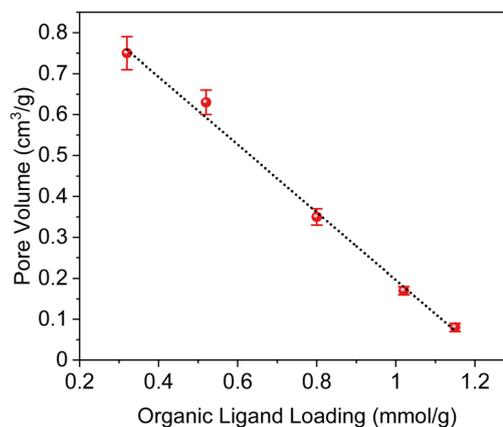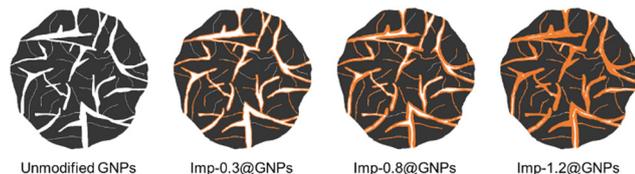
Fig. 9 Schematic representation of the organization of the organic ligand DEHCEBP inserted by impregnation into the meso- and micropores of a graphene nanoplatelet (GNP) support. The macropores in the support are not represented in these drawings.

The diffusive model derivate from Weber and Morris (eqn (7))[73,74] was used to determine how the diffusion inside the porous structure impacts the adsorption process. This highlights the effect of the amount of the ligand into the diffusive process and in the extraction kinetics.

$$q_t = k_{id}t^{1/2} + I \qquad (7)$$

In this equation, q_t is the amount adsorbed at time t, k_{id} is the intra-particle diffusion rate constant (mg g^{-1} h$^{-1/2}$) and I (mg g^{-1}) is a constant related to the thickness of the boundary layer. According to this model, if the relationship between q_t and $t^{1/2}$ is linear and passes through the origin it means that the adsorption process is controlled only by intraparticle diffusion in the liquid phase (inside the pores of the samples). On the other hand, a linear relationship that does not pass through the origin indicates that intraparticle diffusion is involved, but is also indicative of some degree of boundary layer control.[75] Finally, a piecemeal linear relationship indicates that the adsorption process is governed by two or more mechanisms.[76,77]

Fits using this model (eqn (7)) of the kinetics data from the five synthesized materials are shown in Fig. 10.

For materials with DEHCEBP concentrations of 0.8 to 1.2 mmol g^{-1}, three distinct linear sections are observed. Assum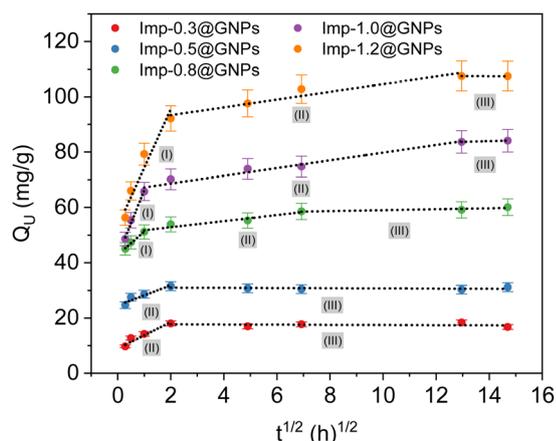ing well-mixed conditions, such that external mass transport resistance can be neglected,[78] the initial linear section (Section I) corresponds to diffusion in the liquid phase (external and in the pore structure); the second section corresponds to intraparticle or diffusion in the boundary layer (here organic layer); and the third section corresponds to the equilibrium state. Section II is the slowest stage in all three cases and is slower in Imp-1.0 and Imp-1.2@GNPs than in Imp-0.8@GNPs. The relationships for the impregnated materials with DEHCEBP concentrations of 0.3 to 0.5 mmol g^{-1} only consist of two sections, with no section I due to high total pore volume. Decreasing the total pore volume by increasing the amount of ligand in the sample leads to an increase of time to reach the end of section I.

The intercept of the intraparticle diffusion Section (II), which is proportional to the thickness of the boundary layer,[77,79] increases with the ligand content of the materials, as does the equilibration time (Table 2). These trends are consistent with the results presented above indicating that the ligand molecules form multiple layers in the pores of the support at concentrations higher than 0.3 mmol g^{-1}. The characteristic rate of adsorption under intraparticle diffusion, k_{id}, decreases from Imp-0.3 to Imp-0.8@GNPs but is similar for Imp-0.8, Imp-1.0 and Imp-1.2@GNPs (Table 2).

Fig. 11 shows that while the uranium extraction capacity of the synthesized materials increases linearly with the ligand concentration, from 18 to 108 mg g^{-1}, the ligand to uranium molar ratio follows the opposite trend. In a previous study, we found that silica-based materials impregnated with DEHCEBP had much lower extraction capacities (from 28 to 54 mg g^{-1}). However they had the same equilibrium ligand to uranium molar ratio (L/U $\sim$ 2) whatever the ligand content was (0.2–0.5 mmol g^{-1}), suggesting minimal hindrance of the silica support in the extractions mechanisms.[16] Here, the higher equilibrium L/U ratios (lower uranium extraction efficiency) at lower ligand concentrations (Fig. 11) point toward a possible chemical or physical interaction between the graphene-based support and the DEHCEBP molecules during extraction processes.

Assuming that the amidophosphonate molecules form, in equilibrium, the same complex with ligand to uranium molar ratios close to 2, regardless of the support on which they are impregnated, it is possible to suppose that some of the ligands present in the GNP-based materials remain inaccessible during extraction. The proportion of inaccessible ligands (τ_{IL}) was

Fig. 10 Weber−Morris intraparticle diffusion plots for U(VI) adsorption by the five impregnated GNPs-based materials with DEHCEBP concentrations of 0.3–1.2 mmol g^{-1}. The different components of the relationships are numbered I, II and III.

Table 2 Uranium extraction parameters of the impregnated GNP materials

Material	$Q_{Umax}{}^{a}$	t^{b}	I^{c}	$k_{id}{}^{d}$
Imp-0.3@GNPs	18 ($\pm$1)	4 hours	8.9	4.8
Imp-0.5@GNPs	31 ($\pm$2)	4 hours	24.6	3.6
Imp-0.8@GNPs	59 ($\pm$3)	2 days	50.6	1.1
Imp-1.0@GNPs	84 ($\pm$4)	7 days	65.9	1.4
Imp-1.2@GNPs	108 ($\pm$5)	7 days	90.6	1.4

^{a} Maximum uranium extraction capacity (mg g^{-1}). ^{b} Estimated equilibration time. ^{c} Y-intercept of the intraparticle diffusion section. ^{d} Rate of adsorption in the intraparticle diffusion domain.
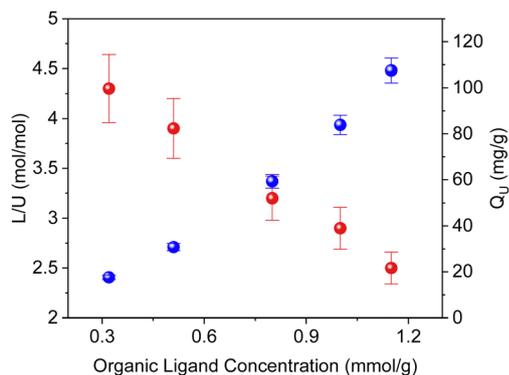
Fig. 11 Equilibrium ligand to uranium molar ratio (red dots) and uranium extraction capacity (blue dots) of the five impregnated materials as a function of the DEHCEBP concentration.

estimated by subtracting the ligand concentration present in each material (τ_L) by the calculated ligand concentration required to reach L/U = 2 ($\tau_{(L/U=2)}$), keeping the experimentally measured Q_U values fixed.

Eqn (8) and (9) are used to calculate the ligand concentration required to reach L/U = 2 and the concentration of the inaccessible ligand, respectively.

$$\tau_{(L/U=2)} = Q_U \times 2 \qquad (8)$$

$$\tau_{IL} = \tau_L - \tau_{(L/U=2)} \qquad (9)$$

The results obtained for each synthesized GNPs-based material are shown in Table 3.

The calculation of the concentration of DEHCEBP molecules (mmol g^{-1}) not involved in U(vi) extraction is the lowest for Imp-0.3 and increases with increasing the concentration of ligand apart from Imp1.2.

There are various hypotheses that can explain the presence of an "unused ligand". The first one would be the inaccessibility of some of ligands due to chemical interactions involving the lone pair of electrons on the phosphorus atom for instance.[67] However as previously explained, the material with the lowest ligand content (0.3) contains enough DEHCEBP to cover the entire surface of the GNPs with a monolayer. This material should have the highest concentration of inaccessible DEHCEBP molecules since it has the highest concentration of

Table 3 Concentration of ligand molecules not involved in U(vi) extraction at equilibrium

Material	$\tau_{LU}{}^a$	Normalized $\tau_{LU}{}^b$
Imp-0.3@GNPs	0.17 ($\pm$0.03)	0.27 ($\pm$0.04)
Imp-0.5@GNPs	0.25 ($\pm$0.03)	0.30 ($\pm$0.04)
Imp-0.8@GNPs	0.30 ($\pm$0.04)	0.32 ($\pm$0.04)
Imp-1.0@GNPs	0.30 ($\pm$0.05)	0.31 ($\pm$0.05)
Imp-1.2@GNPs	0.25 ($\pm$0.05)	0.25 ($\pm$0.05)

^{a} Concentration of DEHCEBP molecules (mmol g^{-1}) not involved in U(vi) extraction. ^{b} Concentration of DEHCEBP molecules (mmol g^{-1}) not involved in U(vi) extraction normalized to the fraction of filled pore volume.

CNPs. This is not the case however (Table 3) thus discarding our first hypothesis.

The second hypothesis assumes the leaching of some of the ligand during the extraction experiments. However, the phosphorus concentration in solution remained stable after 4 h of extraction, at 0, 0.8, 1.9, 1.8 and 2.4 wt% of DEHCEBP loss for the Imp-0.3–Imp-1.2@GNPs materials, respectively (Fig. S6, ESI†). This suggests that only molecules that interact weakly with the graphene support are lost, invalidating our second hypothesis.

The third hypothesis is that the amidophosphonate molecules located in the smaller pores (micropores) remain trapped and do not therefore contribute to uranium extraction. Normalizing the concentrations of inaccessible ligands to the percentage of filled micropore volume (Fig. 7) yields similar values for all the synthesized materials (Table 3), indicating that the loss of uranium extraction efficiency in these materials could indeed be due to a portion of the ligands being trapped in the micropores of the GNPs. The increase in extraction capacity and extraction efficiency with the ligand concentration can therefore be explained by the increase in the absolute and relative concentrations of accessible ligand molecules in the mesopores of the support.

Conclusions

A series of materials were prepared by impregnation of a graphene nanoplatelet support with various concentrations of an amidophosphonate ligand (DEHCEBP). Particle size measurements obtained by laser diffraction and SEM analysis show particle agglomeration probably due to the ligand acting as a bonding agent between initially separated nanoplatelets. While Raman spectroscopy and X-ray diffraction data confirm that the carbon network and interlayer distance of pure GNPs are not modified after impregnation, nitrogen adsorption–desorption curves reveal how this functionalization fundamentally modifies the porous structure of the support. As the ligand concentration increases, the total pore volume decreases. We show also that the DEHCEBP molecules first fill the micropore volume and then the mesopore volume of the GNPs. Increasing the amount of DEHCEBP inside the porous structure leads to the formation of multiple layers at the interface between the pores and the solid phase.

Uranium extraction tests were performed in high sulfate solution as a simulant of ore leaching conditions. Increasing the amount of DEHCEBP in the sample increases the equilibrium time. Fits of the kinetics data with the Weber and Morris model indicate that the increase of the amidophosphonate content leads to an increase of diffusion inside the porous structure and also an increase of the diffusion in the organic layer. These results are in keeping with the decrease of the total pore volume and the multilayer arrangement of the DEHCEBP molecules in the materials with higher ligand concentrations.

Although results suggest that the ligand molecules located inside the micropores do not contribute to uranium extraction,

the amount of accessible ligand in the mesopores increases with the ligand concentration (in absolute and relative terms), and thus the extraction capacity of the materials also increases, reaching 108 mg g^{-1} at 1.2 mmol g^{-1} DEHCEBP. These materials exhibit higher extraction capacities than the silica-based materials we previously studied.

Provided they could be obtained in column-suited shapes, they could therefore be used for solid-phase uranium extraction in acidic solutions with high sulfate concentrations. Several shaping methods for these materials, their amenability to recycling, elution and reuse are currently being studied. We strongly believe that the conclusions drawn in this study can be extended to the impregnation of other organic compounds and their various applications in the field of adsorption.

Author contributions

Aline Dressler: formal analysis, validation, investigation, writing – original draft, writing – review & editing visualization. Antoine Leydier: formal analysis, resources, writing – review & editing visualization, project administration, Agnès Grandjean: formal analysis, supervision, resources, project administration, funding acquisition, writing – review & editing.

Conflicts of interest

There are no conflicts to declare

Acknowledgements

Notes and references

1 I. Ali, *Chem. Rev.*, 2012, **112**, 5073–5091.
2 A. E. Burakov, E. V. Galunin, I. V. Burakova, A. E. Kucherova, S. Agarwal, A. G. Tkachev and V. K. Gupta, *Ecotoxicol. Environ. Saf.*, 2018, **148**, 702–712.
3 N. N. Hidayah and S. Z. Abidin, *Miner. Eng.*, 2017, **112**, 103–113.
4 A. Charlot, F. Cuer and A. Grandjean, *New J. Chem.*, 2017, **41**, 503–511.
5 A. Charlot, T. Dumas, P. L. Solari, F. Cuer and A. Grandjean, *Eur. J. Inorg. Chem.*, 2016, 563–573.
6 A. Charlot, S. E. Mourabit, F. Goettmann, G. Arrachart, R. Turgis and A. Grandjean, *RSC Adv.*, 2014, **4**, 64138–64141.
7 T. Le Nedelec, A. Charlot, F. Calard, F. Cuer, A. Leydier and A. Grandjean, *New J. Chem.*, 2018, **42**, 14300–14307.
8 A. Dressler, T. Le Nedelec, A. Leydier, F. Cuer, T. Dumas and A. Grandjean, *Chem. Eng. J. Adv.*, 2022, **9**, 100225.
9 D. K. Singh, S. Mondal and J. K. Chakravartty, *Solvent Extr. Ion Exch.*, 2016, **34**, 201–225.
10 R. Turgis, A. Leydier, G. Arrachart, F. Burdet, S. Dourdain, G. Bernier, M. Miguirditchian and S. Pellet-Rostaing, *Procedia Eng.*, 2016, **138**, 258–266.
11 P. Baron, G. Bernier, D. Hartmann, C. Laluc and M. Marbet, WO2014/139869, 2014.
12 O. Pecheur, D. Guillaumont, S. Dourdain, L. Berthon, R. Turgis, C. Fillaux, G. Arrachart and F. Testard, *Solvent Extr. Ion Exch.*, 2016, **34**, 260–273.
13 Y. Song, Y. Du, D. Lv, G. Ye and J. Wang, *J. Hazard. Mater.*, 2014, **274**, 221–228.
14 N. Rao, M. Wang, Z. Shang, Y. Hou, G. Fan and J. Li, *Energy Fuels*, 2018, **32**, 670–677.
15 J. A. Cecilia, E. Vilarrasa-García, C. García-Sancho, R. M. A. Saboya, D. C. S. Azevedo, C. L. Cavalcante and E. Rodríguez-Castellón, *Int. J. Greenhouse Gas Control*, 2016, **52**, 344–356.
16 A. Dressler, A. Leydier and A. Grandjean, *Molecules*, 2022, **27**, 4342.
17 K. Lü, G. Zhao and X. Wang, *Chin. Sci. Bull.*, 2012, **57**, 1223–1234.
18 S. Suzuki and M. Yoshimura, *Sci. Rep.*, 2017, **7**, 14851.
19 M. D. Stoller, S. Park, Y. Zhu, J. An and R. S. Ruoff, *Nano Lett.*, 2008, **8**, 3498–3502.
20 C. N. Rao, A. K. Sood, K. S. Subrahmanyam and A. Govindaraj, *Angew. Chem., Int. Ed.*, 2009, **48**, 7752–7777.
21 K. S. Novoselov, V. I. Fal'ko, L. Colombo, P. R. Gellert, M. G. Schwab and K. Kim, *Nature*, 2012, **490**, 192–200.
22 P. Cataldi, A. Athanassiou and I. Bayer, *Appl. Sci.*, 2018, **8**, 1438.
23 R. Sengupta, M. Bhattacharya, S. Bandyopadhyay and A. K. Bhowmick, *Prog. Polym. Sci.*, 2011, **36**, 638–670.
24 S. Dul, L. Fambri, C. Merlini, G. M. O. Barra, M. Bersani, L. Vanzetti and A. Pegoretti, *Polym. Compos.*, 2017, **40**, E285–E300.
25 A. Maniadi, M. Vamvakaki, M. Suchea, I. Tudose, M. Popescu, C. Romanitan, C. Pachiu, O. Ionescu, Z. Viskadourakis, G. Kenanakis and E. Koudoumas, *Materials*, 2020, **13**, 4776.
26 L. Chen, X. Li, E. E. L. Tanner and R. G. Compton, *Chem. Sci.*, 2017, **8**, 4771–4778.
27 C. Zhang, Z. Chen, W. Guo, C. Zhu and Y. Zou, *Int. J. Biol. Macromol.*, 2018, **112**, 1048–1054.
28 L. Ji, W. Chen, Z. Xu, S. Zheng and D. Zhu, *J. Environ. Qual.*, 2013, **42**, 191–198.
29 J. G. Yu, L. Y. Yu, H. Yang, Q. Liu, X. H. Chen, X. Y. Jiang, X. Q. Chen and F. P. Jiao, *Sci. Total Environ*, 2015, **502**, 70–79.
30 L. Kavan, J. H. Yum and M. Grätzel, *ACS Nano*, 2011, **5**, 165–172.
31 I. M. Inuwa, A. Hassan, D.-Y. Wang, S. A. Samsudin, M. K. Mohamad Haafiz, S. L. Wong and M. Jawaid, *Polym. Degrad. Stab.*, 2014, **110**, 137–148.
32 Z.-x Zhang, J.-x Dou, J.-h He, C.-x Xiao, L.-y Shen, J.-h Yang, Y. Wang and Z.-w Zhou, *J. Mater. Chem. C*, 2017, **5**, 4145–4158.
33 Y. Cui, S. I. Kundalwal and S. Kumar, *Carbon*, 2016, **98**, 313–333.

34 A. E. Del Rio Castillo, V. Pellegrini, A. Ansaldo, F. Ricciardella, H. Sun, L. Marasco, J. Buha, Z. Dang, L. Gagliani, E. Lago, N. Curreli, S. Gentiluomo, F. Palazon, M. Prato, R. Oropesa-Nuñez, P. S. Toth, E. Mantero, M. Crugliano, A. Gamucci, A. Tomadin, M. Polini and F. Bonaccorso, *Mater. Horiz.*, 2018, **5**, 890–904.

35 M. Shtein, I. Pri-Bar, M. Varenik and O. Regev, *Anal. Chem.*, 2015, **87**, 4076–4080.

36 T. Kuila, S. Bose, A. K. Mishra, P. Khanra, N. H. Kim and J. H. Lee, *Prog. Mater. Sci.*, 2012, **57**, 1061–1105.

37 V. Georgakilas, M. Otyepka, A. B. Bourlinos, V. Chandra, N. Kim, K. C. Kemp, P. Hobza, R. Zboril and K. S. Kim, *Chem. Rev.*, 2012, **112**, 6156–6214.

38 H. Wang, X. Yuan, Y. Wu, H. Huang, X. Peng, G. Zeng, H. Zhong, J. Liang and M. Ren, *Adv. Colloid Interface Sci.*, 2013, **195–196**, 19–40.

39 D. Lunt, P. Boshoff, M. Boylett and Z. El-Ansary, *J. South. Afr. Inst. Min. Metall.*, 2007, **107**, 419–426.

40 C. R. Edwards and A. J. Oliver, *JOM*, 2000, **52**, 12–20.

41 K. C. Sole, P. M. Cole, A. M. Feather and M. H. Kotze, *Solvent Extr. Ion Exch.*, 2011, **29**, 868–899.

42 L. Dolatyari, M. R. Yaftian and S. Rostamnia, *J. Environ. Manage.*, 2016, **169**, 8–17.

43 J. Płotka-Wasylka, N. Szczepańska, M. de la Guardia and J. Namieśnik, *TrAC, Trends Anal. Chem.*, 2016, **77**, 23–43.

44 J. Veliscek-Carolan, K. A. Jolliffe and T. L. Hanley, *ACS Appl. Mater. Interfaces*, 2013, **5**, 11984–11994.

45 M. F. Cheira, M. N. Rashed, A. E. Mohamed, I. H. Zidan and M. A. Awadallah, *Sep. Sci. Technol.*, 2020, **55**, 3072–3088.

46 S. Yang, J. Qian, L. Kuang and D. Hua, *ACS Appl. Mater. Interfaces*, 2017, **9**, 29337–29344.

47 P. J. Lebed, J.-D. Savoie, J. Florek, F. Bilodeau, D. Larivière and F. Kleitz, *Chem. Mater.*, 2012, **24**, 4166–4176.

48 M. Carboni, C. W. Abney, K. M. L. Taylor-Pashow, J. L. Vivero-Escoto and W. Lin, *Ind. Eng. Chem. Res.*, 2013, **52**, 15187–15197.

49 H. Guo, P. Mei, J. Xiao, X. Huang, A. Ishag and Y. Sun, *Chemosphere*, 2021, **278**, 130411.

50 H. Mohamud, P. Ivanov, B. C. Russell, P. H. Regan and N. I. Ward, *J. Radioanal. Nucl. Chem.*, 2018, **316**, 839–848.

51 M. A. Gado, B. M. Atia, M. F. Cheira, M. E. Elawady and M. Demerdash, *Radiochim. Acta*, 2021, **109**, 743–757.

52 L. Chen, Z. Bai, L. Zhu, L. Zhang, Y. Cai, Y. Li, W. Liu, Y. Wang, L. Chen, J. Diwu, J. Wang, Z. Chai and S. Wang, *ACS Appl. Mater. Interfaces*, 2017, **9**, 32446–32451.

53 L. L. Song, C. Chen, F. Luo, S. Y. Huang, L. L. Wang and N. Zhang, *J. Radioanal. Nucl. Chem.*, 2016, **310**, 317–327.

54 D. Rinsant, E. Andreiadis, M. Carboni and D. Meyer, *Mater. Lett.*, 2019, **253**, 285–288.

55 Y. Cheng, P. He, F. Dong, X. Nie, C. Ding, S. Wang, Y. Zhang, H. Liu and S. Zhou, *Chem. Eng. J.*, 2019, **367**, 198–207.

56 D. Wang, J. Song, J. Wen, Y. Yuan, Z. Liu, S. Lin, H. Wang, H. Wang, S. Zhao, X. Zhao, M. Fang, M. Lei, B. Li, N. Wang, X. Wang and H. Wu, *Adv. Energy Mater.*, 2018, **8**, 1802607.

57 M. Karve and R. V. Rajgor, *Desalination*, 2008, **232**, 191–197.

58 M. Merdivan, M. Z. Düz and C. Hamamci, *Talanta*, 2001, **55**, 639–645.

59 B. M. Atia, Y. M. Khawassek, G. M. Hussein, M. A. Gado, M. A. El-Sheify and M. F. Cheira, *J. Environ. Chem. Eng.*, 2021, **9**, 105726.

60 X. Xu, C. Song, J. M. Andrésen, B. G. Miller and A. W. Scaroni, *Microporous Mesoporous Mater.*, 2003, **62**, 29–45.

61 R. Turgis, A. Leydier, G. Arrachart, F. Burdet, S. Dourdain, G. Bernier, M. Miguirditchian and S. Pellet-Rostaing, *Solvent Extr. Ion Exch.*, 2014, **32**, 685–702.

62 F. Farivar, P. Lay Yap, R. U. Karunagaran and D. Losic, *C*, 2021, **7**, 41.

63 Z. Ni, Y. Wang, T. Yu and Z. Shen, *Nano Res.*, 2010, **1**, 273–291.

64 D. Graf, F. Molitor, K. Ensslin, C. Stampfer, A. Jungen, C. Hierold and L. Wirtz, *Nano Lett.*, 2007, **7**, 238–242.

65 C. Casiraghi, S. Pisana, K. S. Novoselov, A. K. Geim and A. C. Ferrari, *Appl. Phys. Lett.*, 2007, **91**, 233108.

66 A. C. Ferrari, J. C. Meyer, V. Scardaci, C. Casiraghi, M. Lazzeri, F. Mauri, S. Piscanec, D. Jiang, K. S. Novoselov, S. Roth and A. K. Geim, *Phys. Rev. Lett.*, 2006, **97**, 187401.

67 A. Suri, A. K. Chakraborty and K. S. Coleman, *Chem. Mater.*, 2008, **20**, 1705–1709.

68 B. Ahmadi-Moghadam, M. Sharafimasooleh, S. Shadlou and F. Taheri, *Mater. Des.*, 2015, **66**, 142–149.

69 M. K. Rabchinskii, S. D. Saveliev, S. A. Ryzhkov, E. K. Nepomnyashchaya, S. I. Pavlov, M. V. Baidakova and P. N. Brunkov, *J. Phys.: Conf. Ser.*, 2020, **1695**, 012070.

70 F. Wang and L. T. Drzal, *Materials*, 2018, **11**(11), 2137.

71 M. Zhu, J. Wang, B. C. Holloway, R. A. Outlaw, X. Zhao, K. Hou, V. Shutthanandan and D. M. Manos, *Carbon*, 2007, **45**, 2229–2234.

72 M. Thommes, K. Kaneko, A. V. Neimark, J. P. Olivier, F. Rodriguez-Reinoso, J. Rouquerol and K. S. W. Sing, *Pure Appl. Chem.*, 2015, **87**, 1051–1069.

73 J. Weber Walter and J. C. Morris, *J. Sanit. Eng. Div., Am. Soc. Civ. Eng.*, 1963, **89**, 31–59.

74 F.-C. Wu, R.-L. Tseng and R.-S. Juang, *Chem. Eng. J.*, 2009, **153**, 1–8.

75 A. Ozcan, A. S. Ozcan, S. Tunali, T. Akar and I. Kiran, *J. Hazard. Mater.*, 2005, **124**, 200–208.

76 V. Fierro, V. Torné-Fernández, D. Montané and A. Celzard, *Microporous Mesoporous Mater.*, 2008, **111**, 276–284.

77 S. Biswas, T. K. Sen, A. M. Yeneneh and B. C. Meikap, *Sep. Sci. Technol.*, 2018, **54**, 1106–1124.

78 S. Suresh, V. Chandra Srivastava and I. Mani Mishra, *J. Environ. Eng.*, 2011, **137**, 1145–1157.

79 G. McKay, M. S. Otterburn and A. G. Sweeney, *Water Res.*, 1980, **14**, 15–20.